PAPER • OPEN ACCESS

Optical-acoustic excitation of broadband terahertz antiferromagnetic spin waves

New Journal of Physics
The open access journal at the forefront of physics

Deutsche Physikalische Gesellschaft DPG
IOP Institute of Physics

Published in partnership with: Deutsche Physikalische Gesellschaft and the Institute of Physics

OPEN ACCESS

RECEIVED
18 May 2022

REVISED
23 August 2022

ACCEPTED FOR PUBLICATION
30 August 2022

PUBLISHED
15 September 2022

PAPER

Optical-acoustic excitation of broadband terahertz antiferromagnetic spin waves

Jinglin Zhang[1,6], Xu Ge[1,6], Shaojie Yu[1], Lu Yu[1], Diandian Dong[1], Jianhui Song[1], Yangyi Chen[1], JiaPu Li[1], Wei Luo[1], Shiheng Liang[2], Yoshichika Otani[3,4,5], Long You[1], Xiaofei Yang[1] and Yue Zhang[1,*]

[1] School of Optical and Electronic Information, Huazhong University of Science and Technology, Wuhan, People's Republic of China
[2] Department of Physics, Hubei University, Wuhan, People's Republic of China
[3] Institute for Solid State Physics, The University of Tokyo, Japan
[4] Quantum Nano-Scale Magnetism Team, CEMS-RIKEN, Japan
[5] Trans-Scale Quantum Science Institute, The University of Tokyo, Bunkyo-ku, Tokyo 113-0033, Japan
[*] Author to whom any correspondence should be addressed.
[6] The authors who have the same contribution to this work.

E-mail: yue-zhang@hust.edu.cn

Keywords: optical-acoustic transducer, antiferromagnet, terahertz spin wave, Dzyaloshinskii–Moriya interaction

Abstract

We propose an optical-acoustic means to excite *broadband* terahertz antiferromagnetic (AFM) spin wave in a metal/insulator/antiferromagnet heterostructure. The AFM spin wave is excited by an ultrafast strain wave triggered by a femtosecond pulsed laser based on photoacoustic conversion. This spin wave comprises an AFM exchange spin wave and a magnetoelastic spin wave. Their dispersion curves are overlapped in a wide frequency range by manipulating the Dzyaloshinskii–Moriya interaction, which is accompanied by lifting the degeneration of the spin-wave modes with opposite chirality. This optical-acoustic excitation of spin waves exploits the laser-induced ultrafast strain waves and avoids the thermal effect from the laser. It paves a way to develop novel AFM devices that can apply for ultrafast information processing and communication.

1. Introduction

Terahertz (THz) radiation (electromagnetic (EM) radiation with frequency ranging from 0.3 to 3 THz) attracts extensive interest owing to its unique properties and extraordinary potential applications [1]. For example, THz waves can penetrate an optically opaque medium with a great signal-noise ratio, valuable in high-resolution imaging, wireless communication, and security check [2]. THz waves are also safe in biomedical applications due to low photon energy [3].

A strong antiferromagnetic (AFM) exchange field sustains THz magnetization precession in an AFM medium, generating THz EM waves [4]. This THz precession is triggered by the interaction between the EM field of a femtosecond (fs) laser and the AFM moments [4–8]. In addition to a uniform AFM precession, Hortensius *et al* also realized generation and detection of a coherent broadband AFM spin-wave propagation excited by an ultrashort pulse of laser [9]. However, the laser transmission in an optically transparent AFM medium may bring about a thermal effect that weakens the exchange coupling [10]. This is especially problematic for a metallic AFM medium. In recent years, efforts have been paid to non-thermal excitation of ultrafast magnetization precession [11], such as ultrafast AFM dynamics via light-driven phonons [12] and ultrafast manipulation of magnetic parameters by photo-electron interaction [13, 14].

In addition to laser, a picosecond (ps) strain wave may also induce THz magnetization dynamics [15]. Barra *et al* have predicted THz AFM dynamics induced by a transient ps strain wave based on the inverse piezoelectric effect via switching on a DC voltage source [16]. This technique avoids the thermal effect from the laser but cannot trigger continuous THz emission.

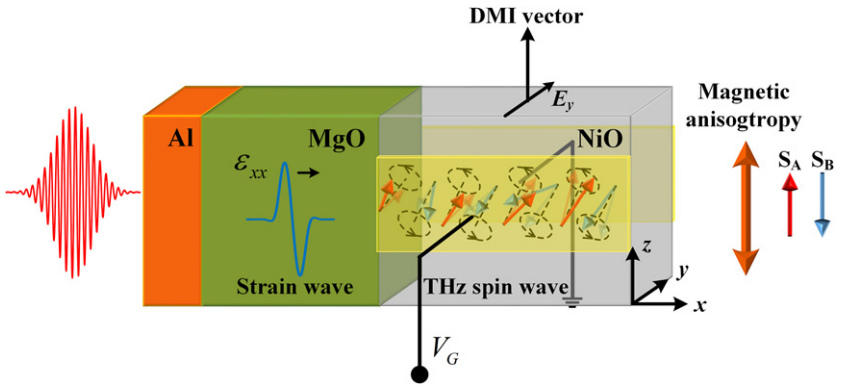

Figure 1. Schematic of a metal/insulator/antiferromagnet heterostructure. The thermal expansion of Al induced by an fs laser generates an ultrafast strain wave propagating through MgO to NiO. This strain wave excites a THz AFM spin wave. The spin-wave frequency is manipulated by the electric field applied between the two electrodes on the opposite sides of NiO. This electric field breaks the inversion symmetry along the *y*-axis direction and generates DMI that shifts the dispersion curve of the AFM exchange spin wave. The magnetic anisotropy constant, DMI vector, and the electric field are all indicated.

An optoacoustic transducer can excite continuous ultrafast magnetization dynamics without laser-induced thermal effect, converting laser thermal energy to mechanical energy to trigger continuous ultrafast strain waves, and thus magnetization precession [17, 18]. A typical device for this optical-acoustic excitation of magnetization dynamics is a metal/insulator/magnet heterostructure [19, 20]. An fs laser irradiates the metal layer, exciting ultrafast thermal expansion that generates a strain wave. The insulator transmits the strain wave but blocks the heat conduction. The magnetic moments start to process after the strain wave reaches the magnetic medium. Based on this consideration, the optical-acoustic excitation of magnetization switching and THz FM spin waves has been proposed [20–22]. In general, this spin wave consists of an exchange spin-wave component and a magnetoelastic one, and the intersections of the dispersion curves of these two spin-wave components determine the spin-wave frequency [20]. The exchange spin wave displays a parabolic dispersion curve in ferromagnets, while the magnetoelastic spin wave has a linear dispersion curve crossing the origin. Therefore, there are only 1–2 intersection points, limiting the frequency range for the application of spin waves.

Unlike an FM spin wave, an AFM exchange spin wave exhibits a hyperbolic dispersion curve that approaches linear at high wavenumbers. On the other hand, the dispersion curve for an AFM exchange spin wave can also be shifted by manipulating the Dzyaloshinskii–Moriya interaction (DMI) [23]. In this way, the dispersion curve of an AFM exchange spin wave may be overlapped with that of a magnetoelastic spin wave in a wide frequency range. We propose optical-acoustic excitation of a broadband THz AFM spin wave in a metal/dielectric/antiferromagnets heterostructure based on this motivation.

2. Model and method

We consider an Al (10 nm)/MgO (400 nm)/NiO (400 nm) heterostructure (figure 1). Here Al converts the heat of an fs laser (800 nm wavelength, 20 fs pulse width, and 3.1 mJ cm^{-2} pulse energy) to an ultrafast strain wave. MgO assists the strain-wave transmission but prevents thermal spreading into NiO. Here NiO is an ideal medium for a strain-induced spin-wave emitter owing to its large magnetostrictive coefficient (140 ppm) [24]. Thanks to the insulating property, an electric field can be applied on NiO to break the structural symmetry along the y-axis direction, which generates a DMI vector along the z-axis direction [25–27] and shifts the dispersion curve of the spin wave propagating along the x-axis direction [23]. A voltage is applied across NiO through the electrodes at the two sides of NiO.

We formulated an atomistic spin model to calculate the magnetization dynamics of an AFM chain composed of two FM sublattices. The discrete energy of an AFM chain is expressed as [28]:

$$E_m = J_a \sum_i \vec{S}^{(i)} \cdot \vec{S}^{(i+1)} - K_a \sum_i (\vec{S}^{(i)} \cdot \vec{e}_z)^2 - D_a \sum_i \vec{e}_z \cdot (\vec{S}^{(i)} \times \vec{S}^{(i+1)}) + \sum_i \left\{ \left[\sum_s B_{1a} \left(S_s^{(i)}\right)^2 \varepsilon_{ss} \right] + \left[\sum_{s \neq p} B_{2a} S_s^{(i)} S_p^{(i)} \varepsilon_{sp} \right] \right\}. \quad (1)$$

Here $\vec{S}^{(i)}$ is the normalized spin magnetic moment at site i [i.e., $\left|\vec{S}^{(i)}\right| = 1$], and $S^{(i)}_{s(p)}$ ($s, p = x, y, z$) is the $s(p)$ component of $\vec{S}^{(i)}$. The first to the fourth terms represent exchange energy, anisotropy energy, DMI energy, and magnetoelastic energy, respectively. The parameters J_a, K_a, D_a, B_{1a}, and B_{2a} are AFM exchange integral, easy-axis anisotropy energy, DMI energy, the first- and second-order magnetoelastic energy, respectively. For simplicity, we considered a polycrystalline or amorphous medium with a uniaxial anisotropy [29, 30]. The expression for the magnetoelastic energy in equation (1) is suitable for either an FM medium or an AFM one with a cubic structure [16, 31–33]. For a polycrystalline or amorphous medium, the magnetoelastic energy in equation (1) should be approximated as $\sum_i B_{1a}\left(S^{(i)}_s\right)^2\varepsilon_{xx}$ since $B_{1a} = B_{2a}$ and $\varepsilon_{sp} = 0$ except for $s = p = x$ [33, 34].

We numerically solved the atomistic Landau–Liftshitz–Gilbert equation [35]:

$$\frac{\partial\vec{S}^{(i)}}{\partial t} = -\gamma\vec{S}^{(i)}\times\vec{H}^{(i)}_{\text{eff}} + \alpha\vec{S}^{(i)}\times\frac{\partial\vec{S}^{(i)}}{\partial t}, \tag{2}$$

where γ is the gyromagnetic ratio. In equation (2), α is the Gilbert damping parameter. $\vec{H}^{(i)}_{\text{eff}}$ is the effective magnetic field that is related to the magnetic potential energy by $\vec{H}^{(i)}_{\text{eff}} = -\frac{1}{\mu_0 m}\frac{\partial E_m}{\partial\vec{S}^{(i)}}$, where μ_0 is the vacuum permeability, and m is the magnetic moment in a unit cell and written as $m = M_S d^3$ with M_S the saturation magnetization and d the lattice constant. The $\vec{H}^{(i)}_{\text{eff}}$ consisting of the exchange field $\vec{H}^{(i)}_{\text{ex}}$, the anisotropy field $\vec{H}^{(i)}_{\text{K}}$, the DMI induced field $\vec{H}^{(i)}_{\text{D}}$, and the magnetoelastic field $\vec{H}^{(i)}_{\text{ME}}$ can be derived from equation (1) as $\vec{H}^{(i)}_{\text{ex}} = -\frac{J_a}{\mu_0 m}(\vec{S}_{i+1} + \vec{S}_{i-1})$, and $\vec{H}^{(i)}_{\text{K}} = \frac{2}{\mu_0 m}K_a S^{(i)}_z\vec{e}_z$, and $\vec{H}^{(i)}_{\text{D}} = -\frac{1}{\mu_0 m}D_a\vec{e}_z\times\left(\vec{S}_{i+1} - \vec{S}_{i-1}\right)$, and $\vec{H}^{(i)}_{\text{ME}} = -\frac{2}{\mu_0 m}B_{1a}S^{(i)}_x\varepsilon_{xx}\vec{e}_x$ with $B_{1a} = -1.5\lambda_{100}(c_{11} - c_{12})d^3$ (λ_{100} is saturation magnetostrictive coefficient, and c_{11} and c_{12} are elastic stiffness coefficients).

In the effective field for the exchange coupling and DMI, we only consider the contribution from the nearest magnetic moments. We used the rule for a triple scalar product to derive the DMI effective field for the magnetic moment at site i as follows: $E^{(i)}_{\text{D}} = D_a\vec{e}_z\cdot(\vec{S}^{(i)}\times\vec{S}^{(i+1)} - \vec{S}^{(i)}\times\vec{S}^{(i-1)}) = D_a\vec{e}_z\cdot\vec{S}^{(i)}\times(\vec{S}^{(i+1)} - \vec{S}^{(i-1)}) = D_a\vec{S}^{(i)}\cdot[(\vec{S}^{(i+1)} - \vec{S}^{(i-1)})\times\vec{e}_z]$. Since the total AFM magnetization is negligible, the Néel vector $\vec{n} = (\vec{S}_i - \vec{S}_{i-1})/2$ was introduced as the fundamental quantity for the AFM magnetization dynamics.

The strain of NiO originates from the laser-induced thermal expansion of Al and MgO. The dynamics of the thermal expansion is calculated by [36]:

$$\rho\frac{\partial^2 u_x}{\partial t^2} = c_{11}\frac{\partial^2 u_x}{\partial x^2} - 3\beta B\frac{\partial\delta T_l}{\partial x}, \tag{3}$$

where u_x is the displacement along the x-axis direction, and ε_{xx} is defined as: $\varepsilon_{xx} = \frac{\partial u_x}{\partial x}$. ρ, β and B are the density, thermal expansion coefficient, and bulk modulus of Al and MgO, respectively. T_l is the lattice temperature determined by the interaction between the laser and Al. The incident photons excite hot electrons that interfere with phonons and transfer the energy to lattice. This process is described by a two-temperature model [37]:

$$C_\text{e}\frac{\partial T_\text{e}}{\partial t} = \kappa_\text{e}\frac{\partial}{\partial x}\left(\frac{\partial T_\text{e}}{\partial x}\right) - G(T_\text{e} - T_\text{l}) + Q(x,t); \tag{4}$$

$$C_\text{l}\frac{\partial T_\text{l}}{\partial t} = \kappa_\text{l}\frac{\partial}{\partial x}\left(\frac{\partial T_\text{l}}{\partial x}\right) + G(T_\text{e} - T_\text{l}). \tag{5}$$

Here C_e and C_l are the thermal capacities of electrons and lattice, respectively. $C_\text{e} \approx \gamma_\text{e}T_\text{e}$ for temperature far below Fermi temperature. κ_e is the electronic thermal conductivity. As compared to κ_e, the lattice thermal conductivity κ_l is negligible [38]. G is an electron–phonon coupling constant. Q depicts the energy distribution of a Gaussian laser beam as: $Q = 2\sqrt{\frac{\ln 2}{\pi}}\frac{(1-R)}{t_\text{p}\delta}I_0\ \exp\left(-\frac{x}{\delta} - 4\ \ln 2\frac{(t-t_\text{p})^2}{t_\text{p}^2}\right)$ where R is reflectivity, and δ is optical absorption depth, and t_p is the duration of the laser pulse, and I_0 is pulse energy (the energy density for a single pulse of the laser) [39, 40].

In calculating the thermal expansion of Al and MgO, we focused on the laser-induced deformation without considering the magnetostrictive stress of NiO [20]. While in calculating the magnetostrictive stress of NiO, the thermal expansion is neglected owing to the thermal blocking by MgO. Under this assumption, the dynamics of the displacement of NiO is expressed as:

$$\rho\frac{\partial^2 u_x}{\partial t^2} = c_{11}\frac{\partial^2 u_x}{\partial x^2} - \frac{B_{1a}}{d^3}\frac{\partial\left(m_x^2\right)}{\partial x}. \tag{6}$$

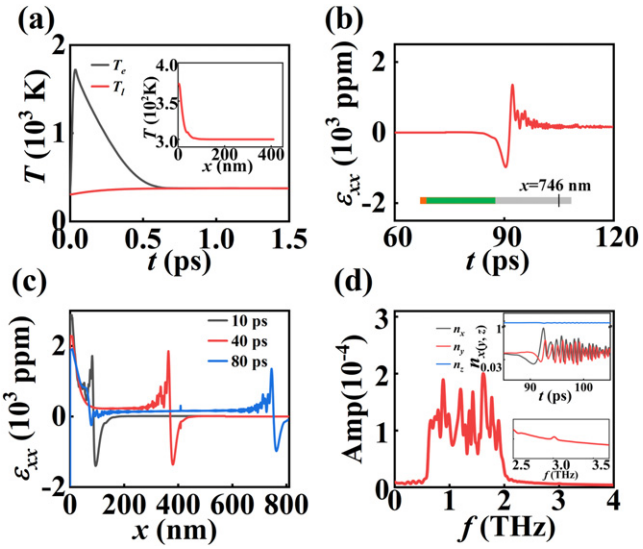

Figure 2. Optical-acoustic excitation of a broadband THz AFM spin wave. (a) Profiles of lattice temperature (T_l, the red line) and electronic temperature (T_e, the black line) at the left edge of Al ($x = 0$ nm). Inset: T_l as a function of x at $t = 10$ ps. (b) Time-dependent ε_{xx} at $x = 746$ nm. Here $t = 0$ ps is defined as when the laser hits the heterostructure. (c) ε_{xx} as a function of x at $t = 10$, 40, and 80 ps. (d) Spectrum for the oscillation of n_y at $x = 746$ nm by fast Fourier transformation. Upper inset: oscillation of the x, y, and z components of an AFM Néel vector at $x = 746$ nm. Lower inset: enlarged spectrum near $f = 3$ GHz.

The parameters for solving equations (2)–(6) are as follows: $\gamma_e = 135$ J K^{-2} m^{-3}, $k_e = 238$ W K^{-1} m^{-1}, $C_l = 2.43 \times 10^6$ J K^{-1} m^{-3}, $R = 0.852$, $\delta = 16.9$ nm [41], $G = 5.69 \times 10^{17}$ W K^{-1} m^{-3} [42], $\beta_{Al} = 2.3 \times 10^{-5}$ K^{-1} [43], $\rho_{Al} = 2700$ kg m^{-3}, $c_{11}^{Al} = 107$ GPa, $c_{12}^{Al} = 61$ GPa, $c_{44}^{Al} = 28$ GPa [44], $\rho_{MgO} = 3580$ kg m^{-3}, $c_{11}^{MgO} = 297$ GPa, $c_{12}^{MgO} = 96$ GPa, $c_{44}^{MgO} = 156$ GPa [45], $\beta_{MgO} = 3.11 \times 10^{-5}$ K^{-1} [46], $\rho_{NiO} = 6828$ kg m^{-3}, $c_{11}^{NiO} = 342.7$ GPa, $c_{12}^{NiO} = 141.3$ GPa [47], $J_a = 4.7 \times 10^{-2}$ eV [48], $M_S = 3.51 \times 10^5$ A m^{-1} [48], $d = 0.42$ nm [28], $\lambda = 140$ ppm [24], $\gamma = 1.76 \times 10^{11}$ rad s^{-1} T^{-1}, $K_a = 2.2 \times 10^{-4}$ eV [28], $\alpha = 1 \times 10^{-3}$. D_a is between 0 and 2×10^{-3} eV [27, 49].

Equations (2)–(6) were numerically solved using a typical Runge–Kutta method with a time step of 0.1 fs. The Al (10 nm)/MgO (400 nm)/NiO (400 nm) heterostructure is discretized into cubic cells with a size of 0.42 nm for NiO and 1 nm for Al and MgO. We exploited a continuity boundary condition at the Al/MgO and MgO/NiO interfaces. A high damping coefficient and acoustic absorbing boundary condition were posed at the right edge of NiO to suppress the reflection of spin waves and strain waves. We assume a slight deviation of $\vec{S}^{(i)}$ from the z-axis by about 3° as an initial condition.

3. Results and discussion

Figure 2(a) depicts the spatiotemporal temperature of the heterostructure under an fs laser. T_e is dominant over T_l, and the rising of T_e is localized in Al and MgO (inset of figure 2(a)). This result means that MgO successfully blocks the thermal diffusion into NiO. The laser-induced thermal expansion triggers the strain-wave propagating from Al to NiO with negligible reflection and decaying (figures 2(b) and (c)). The Néel vector starts to process as soon as the strain wave arrives at the left edge of NiO at around 100 ps (figures 2(c) and (d)). The temporal variation of n_y at $x = 746$ nm is converted into a spectrum using the fast Fourier transformation (FFT, the sampling interval is 1×10^{-16} s) (figure 2(d)). The spectrum illustrates the n_y oscillating in a broad frequency band ranging from 0.5 THz to 2 THz and at a single frequency for a very weak peak around 3 THz. This behavior is different from the single-frequency FM spin wave by optical-acoustic excitation [20–22].

To explain the broadband of spin wave, we deduced the dispersion curve by 2D FFT (figures 3(a)–(c)). The dispersion curve for the magnetoelastic spin wave fits $f = v_s k/2\pi$ with v_s the longitudinal sound velocity of NiO ($v_s = \sqrt{c_{11}/\rho}$) [20]. By using the method in reference [50], we derived the theoretical dispersion for the exchange spin wave: $f_{\pm} = \sqrt{a\gamma^2\left(\tilde{A}k^2 \mp Dk + K_z\right)}/2\pi$, where $a = \frac{A}{2d^2 \cdot M_s^2}$, $\tilde{A} = A - \frac{L^2}{a}$ with $L = \frac{A}{2M_s \cdot d}$, $D = \frac{4D_a}{d^2}$, and $K_z = \frac{4K_a}{d^3}$. Here $f_{+(-)}$ is the frequency for the right (left)-handed spin-wave mode. One can see that the simulated dispersion curve for an exchange spin wave satisfies the derived one at a low and moderate k. At a high k, the simulated dispersion deviates from the derived formula and the

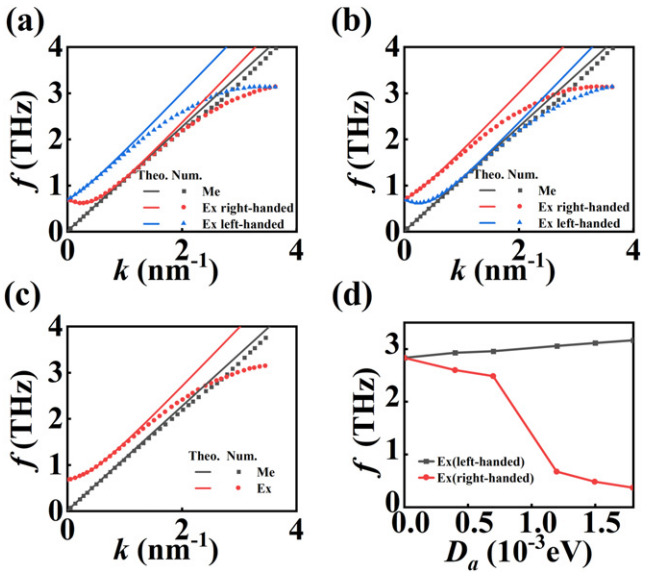

Figure 3. Frequency modulation of the broadband THz AFM spin wave. (a) Dispersion curves of the magnetoelastic (Me) spin wave (black) and exchange (Ex) spin-wave with right-handed component (red) and left-handed one (blue). (In (a)–(c), the solid lines indicate the derived dispersion relationship and the dots denote the numerical results based on the 2D FFT.). The dispersion curves for the magnetoelastic spin wave are overlapped with that of the right-handed exchange spin wave between 0.5–2 THz and intersect with the left-handed one at 3 THz. Here $D = 0.96$ meV. (b) The spin-wave dispersion curve under D that is opposite to (a). (c) The spin-wave dispersion curve for zero D. (d) Frequency modulation for the right- and left-handed exchange spin wave by DMI.

frequency approaches a saturation value, since the wavelength approaches the limit of the cell size. This is consistent with the reported result of atomistic simulation [49].

Under zero DMI, the exchange spin wave has a hyperbolic-type dispersion curve with a gap at $k = 0$, while the magnetoelastic spin wave dispersion is a straight line crossing the origin. In this case, there is only one intersection for these two dispersion curves (figure 3(c)). Nevertheless, under a positive (negative) D, the dispersion curve of the right (left)-handed mode shifts right and overlaps with that of magnetoelastic spin wave in a wide frequency range (from 0.5 THz to 2 THz) (figures 3(a) and (b)). While the dispersion curve of the left-handed (right-handed) mode still intersects with that of the exchange spin wave at a single frequency (3 THz). On the other hand, the increase of D also raises the frequency of the left-handed mode but lowers that of the right-handed one, enlarging the frequency gap between the two modes (figure 3(d)).

The original AFM spin waves are composed of opposite chirality components (figure 4(a)). These two spin-wave components can be separated using an analog low-pass and high-pass filter (inset of figure 4(a)). We simulated this mode filtering for the oscillation of Δn_x and Δn_y at $x = 746$ nm for $D = 1.55$ meV. ($\Delta n_{x(y)} = n_{x(y)} - n_{x(y)0}$ with $n_{x(y)0}$ the initial $x(y)$ component of Néel vector for exhibiting the oscillation amplitude.) The low-frequency ($f = 0.48$ THz) oscillation of Δn_x and Δn_y and the (Δn_x, Δn_y) trajectory show right-handed precession (figures 4(b) and (c)). While the spin wave is passing, the high-pass filter exhibits left-handed precession with slower decaying (figures 4(d) and (e)). However, the strength for the left-handed precession is significantly weaker than that of the right-handed one by several magnitudes. This indicates that the AFM spin wave exhibits almost a single chirality tuned by an external electric field. This chiral spin wave can be exploited in information storage and computation.

Finally, we briefly discuss about the feasibility of the proposed design. We estimated the voltage for generating the DMI vector based on the formula [27]: $\vec{D}_a = -J_a \frac{ed}{E_{SO}} \vec{E} \times \vec{e}_{12}$. Here J_a, e, d, E_{SO}, $\vec{E}$, and $\vec{e}_{12}$ are the exchange integral (4.7×10^{-2} eV), the charge of an electron (1.6×10^{-19} C), the lattice constant (0.42 nm), the energy of spin–orbit coupling, the electric-field strength, and the unit vector for connecting two neighboring sites, respectively. The E_{SO} is given by $E_{SO} = \frac{\hbar^2}{2m_e\lambda^2}$, where $\hbar$ is the reduced Plank constant, m_e is the mass of the electron, and λ is the spin-orbital coupling constant. E_{SO} is typically on the order of 1 eV [25]. Based on the parameters and device dimension, we show that to generate a D_a of 1×10^{-3} eV, the electric-field strength and the applied voltage are at the magnitude of 10^7 V m^{-1} and V, respectively. This is close to the estimation about the DMI energy of an insulating AFM medium by Wang *et al* [51] and Kim *et al* [52].

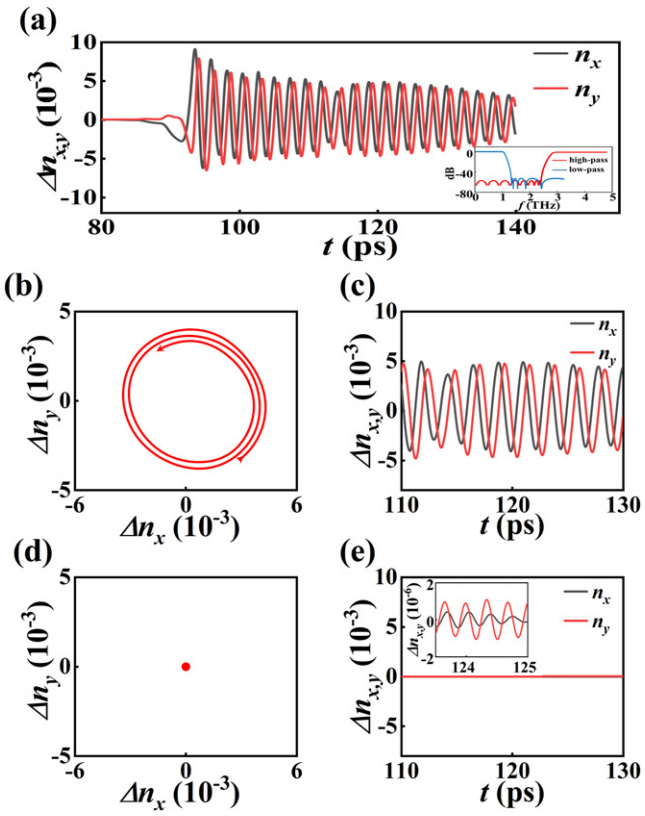

Figure 4. Separation of the spin waves with opposite chirality. (a) Oscillation of n_x and n_y at $x = 746$ nm. Here Δn_x and Δn_y denote the variation of n_x and n_y as compared to the initial values, and they exhibit the oscillation amplitude. Inset: schematic of low-pass and high-pass filters for separating the spin-wave components with opposite chirality. (b) and (c) Oscillation and 2D trajectory of $(\Delta n_x, \Delta n_y)$ for the low-frequency (0.48 THz) spin wave. (d) and (e) Oscillation and 2D trajectory of $(\Delta n_x, \Delta n_y)$ for the high-frequency (3.1 THz) spin wave.

4. Conclusion

We propose broadband THz AFM spin-wave excitation based on optoacoustic conversion in Al/MgO/NiO heterostructure. The spin-wave frequency is determined by the intersection of the dispersion curve of an AFM exchange spin wave and that of a magnetoelastic one. By manipulating DMI, the dispersion curves of these two spin-wave components can overlap in a wide frequency range, and analog low-pass and high-pass filters can separate the two spin-wave components with opposite chirality. This work paves a way to develop an ultrafast AFM information device for storage and computation.

Acknowledgments

The authors acknowledge financial support from the National Key Research and Development Program of China (No. 2022YFE0103300), the National Innovation and Entrepreneurship Training Program for College Students (Nos. 202210487061, 202110487005), and the National Natural Science Foundation of China (Nos. 51971098, U2141236).

Data availability statement

The data that support the findings of this study are available upon reasonable request from the authors.

ORCID iDs

Jinglin Zhang https://orcid.org/0000-0002-9190-6726
Shiheng Liang https://orcid.org/0000-0002-2133-2659

Yoshichika Otani https://orcid.org/0000-0001-8008-1493
Yue Zhang https://orcid.org/0000-0002-1994-3071

References

[1] Mittleman D *et al* 2003 *Introduction in Sensing with Terahertz Radiation* (Berlin: Springer)
[2] Mukherjee P and Gupta B 2008 *Int. J. Infrared Milli Waves* **29** 1091–102
[3] Zaytsev K I *et al* 2019 *J. Opt.* **22** 013001
[4] Satoh T *et al* 2010 *Phys. Rev. Lett.* **105** 077402
[5] Kimel A V, Kirilyuk A, Usachev P A, Pisarev R V, Balbashov A M and Rasing T 2005 *Nature* **435** 655–7
[6] van der Ziel J P, Pershan P S and Malmstrom L D 1965 *Phys. Rev. Lett.* **15** 190–3
[7] Kampfrath T *et al* 2011 *Nat. Photon.* **5** 31–4
[8] Chefonov O V, Ovchinnikov A V, Hauri C P and Agranat M B 2019 *Opt. Express* **27** 27273–81
[9] Hortensius J R, Afanasiev D, Matthiesen M, Leenders R, Citro R, Kimel A V, Mikhaylovskiy R V, Ivanov B A and Caviglia A D 2021 *Nat. Phys.* **17** 1001–6
[10] Ivanov B A 2014 *Low Temp. Phys.* **40** 91–105
[11] Němec P, Fiebig M, Kampfrath T and Kimel A V 2018 *Nat. Phys.* **14** 229–41
[12] Afanasiev D, Hortensius J R, Ivanov B A, Sasani A, Bousquet E, Blanter Y M, Mikhaylovskiy R V, Kimel A V and Caviglia A D 2021 *Nat. Mater.* **20** 607–11
[13] Afanasiev D *et al* 2021 *Sci. Adv.* **7** eabf3096
[14] Mikhaylovskiy R V, Huisman T J, Gavrichkov V A, Polukeev S I, Ovchinnikov S G, Afanasiev D, Pisarev R V, Rasing T and Kimel A V 2020 *Phys. Rev. Lett.* **125** 157201
[15] Kim J-W, Vomir M and Bigot J-Y 2012 *Phys. Rev. Lett.* **109** 166601
[16] Barra A, Domann J, Kim K W and Carman G 2018 *Phys. Rev. Appl.* **9** 034017
[17] Temnov V V 2012 *Nat. Photon.* **6** 728–36
[18] Thevenard L, Peronne E, Gourdon C, Testelin C, Cubukcu M, Charron E, Vincent S, Lemaître A and Perrin B 2010 *Phys. Rev.* B **82** 104422
[19] Kovalenko O, Pezeril T and Temnov V V 2013 *Phys. Rev. Lett.* **110** 266602
[20] Zhuang S H, Meisenheimer P B, Heron J and Hu J M 2021 *ACS Appl. Mater. Interfaces* **13** 48997–9006
[21] Scherbakov A V *et al* 2010 *Phys. Rev. Lett.* **105** 117204
[22] Jäger J V *et al* 2013 *Appl. Phys. Lett.* **103** 032409
[23] Proskurin I, Stamps R L, Ovchinnikov A S and Kishine J-i 2017 *Phys. Rev. Lett.* **119** 177202
[24] Phillips T G and White R L 1967 *Phys. Rev.* **153** 616–20
[25] Cheng R, Daniels M W, Zhu J-G and Xiao D 2016 *Sci. Rep.* **6** 24223
[26] Daniels M W, Cheng R, Yu W, Xiao J and Xiao D 2018 *Phys. Rev.* B **98** 134450
[27] Liu T and Vignale G 2011 *Phys. Rev. Lett.* **106** 247203
[28] Shiino T, Oh S H, Haney P M, Lee S W, Go G, Park B G and Lee K J 2016 *Phys. Rev. Lett.* **117** 087203
[29] Hindmarch A T, Rushforth A W, Campion R P, Marrows C H and Gallagher B L 2011 *Phys. Rev.* B **83** 212404
[30] Kateb M and Ingvarsson S 2021 *J. Magn. Magn. Mater.* **532** 167982
[31] Nussle T, Thibaudeau P and Nicolis S 2019 *J. Magn. Magn. Mater.* **469** 633–7
[32] Popov P A, Safin A R, Kirilyuk A, Nikitov S A, Lisenkov I, Tyberkevich V and Slavin A 2020 *Phys. Rev. Appl.* **13** 044080
[33] Consolo G, Valenti G, Safin A R, Nikitov S A, Tyberkevich V and Slavin A 2021 *Phys. Rev.* B **103** 134431
[34] Chen F *et al* 2021 *Phys. Rev. Appl.* **15** 014030
[35] Gilbert T L 2014 *IEEE Trans. Magn.* **40** 3443–9
[36] Wright O B and Gusev V E 1995 *IEEE Trans. Ultrason. Ferroelectr. Freq. Control* **42** 331–8
[37] Sun C-K, Vallée F, Acioli L H, Ippen E P and Fujimoto J G 1994 *Phys. Rev.* B **50** 15337
[38] Valette S, Le Harzic R, Huot N, Audouard E and Fortunier R 2005 *Appl. Surf. Sci.* **247** 238–42
[39] Wang X, Ye X, Yao H, Wei P, Yin F, Cong J, Tong Y, Zhang L and Zhu W 2021 *J. Laser Appl.* **33** 0000264
[40] Majchrzak E and Dziatkiewicz J 2012 *Sci. Res. Inst. Math. Comp. Sci.* **11** 63–70
[41] Valette S 2003 PhD Thesis Université Jean Monnet - Saint-Etienne
[42] Zhu X 2000 *Appl. Surf. Sci.* **167** 230
[43] Hagart-Alexander C 2010 *Instrumentation Reference Book* 4th edn (Boston, MA: Butterworth-Heinemann)
[44] Gerlich D and Fisher E S 1969 *J. Phys. Chem. Solids* **30** 1197–205
[45] Sumino Y, Anderson O L and Suzuki I 1983 *Phys. Chem. Miner.* **9** 38–47
[46] Chopelas A 1990 *Phys. Chem. Miner.* **17** 142–8
[47] Jifang W, Fisher E S and Manghnzmi M H 1991 *Chin. Phys. Lett.* **8** 153–6
[48] Lee K *et al* 2021 *Nat. Nanotechnol.* **16** 1337–41
[49] José dos Santos F, dos Santos Dias M and Lounis S 2020 *Phys. Rev.* B **102** 104436
[50] Tveten E G, Müller T, Linder J and Brataas A 2016 *Phys. Rev.* B **93** 104408
[51] Wang X-g, Chotorlishvili L, Guo G-h and Berakdar J 2018 *J. Appl. Phys.* **124** 073903
[52] Kim T H, Han S H and Cho B K 2019 *Commun. Phys.* **2** 41